PHYSICAL REVIEW B VOLUME 40, NUMBER 17 15 DECEMBER 1989-I

Molecular-dynamics studies of the growth modes and structure of amorphous silicon films via atom deposition

W. D. Luedtke and Uzi Landman
School of Physics, Georgia Institute of Technology, Atlanta, Georgia 30332-0430
(Received 7 April 1989; revised manuscript received 11 July 1989)

The growth modes of amorphous silicon (*a*-Si) films via vapor-phase and low-energy molecular-beam epitaxy are investigated with use of molecular-dynamics simulations. In these simulations, realistic interatomic interaction potentials, which include two- and three-body interactions, are employed. The dependencies of the growth mechanism and structure of the grown amorphous film on the method of deposition are investigated. For deposition normal to a (111) crystalline Si substrate, a uniform *a*-Si film is generated. Deposition using a beam directed at 60° from the normal to the substrate results in preferential orientation of density inhomogeneities corresponding to a columnar microstructure in the film, while deposition where the impinging particles arrive at random directions to the substrate yields an *a*-Si film containing microvoids. The structural characteristics of the amorphous material and of the interface between the crystal and the amorphous film are analyzed.

I. INTRODUCTION

Investigations of the fundamental mechanisms of crystal-growth processes are of great interest from both basic science and technological perspectives. Recent technological advances, particularly in microelectronics, optics, and other thin-film-based technologies, where the dependencies of the system (or device) properties and response on the physical structure are critical issues, provide the impetus for intensive research efforts aimed at understanding and elucidating the complex relationships between the operational and structural characteristics and the dependence of the latter on the method of growth.[1-7] From the basic science perspective, studies of crystal-growth processes provide opportunities for integrated approaches based on statistical-mechanical formulations of nonequilibrium phenomena, phase transitions and nucleation kinetics, surface-science techniques, solid-state methodologies, and computer simulations of materials phenomena.

Crystal growth from the melt or via direct condensation of vapor atoms onto a cold substrate have been observed and used for many years. Among the various crystal-growth techniques which are currently used, epitaxial growth from the vapor phase and in particular, growth via molecular-beam epitaxy (MBE) play a major role.[1-7] Furthermore, employing an arsenal of physical characterization techniques, it has been demonstrated in numerous cases that the structural properties of the fabricated samples, on various levels of microscopic detail, and thus the physical properties (electrical, magnetic, optical, and mechanical) exhibited by the materials, depend in a critical way on the method of growth and the parameters which control the growth process (such as substrate and vapor temperatures, angle of incidence of the beam, incident fluxes, and substrate morphology).

While much experimental work has been done on vapor-phase and molecular-beam epitaxy,[1-7] the available theoretical approaches to these problems are phenomenological in nature due to their complex many-body character.[8] On the other hand, computer simulations, where the evolution of a physical system is simulated, with refined temporal and spatial resolution, alleviate certain of the difficulties which hamper other theoretical approaches, particularly for complex systems characterized by a large number of degrees of freedom, lack of symmetry, nonlinearities, and complicated interactions. Recent progress in large-scale computing coupled with advances in the development of realistic interaction potentials[9,10] have opened new avenues for the investigation of the microscopic origins of material phenomena.[9-14] In particular, molecular-dynamics (MD) simulations, where the system evolution is followed via direct numerical solution of the particle's equations of motion, have been applied to liquid-[9,10,15-19] and vapor-phase[9,20-26] epitaxial-growth problems, yielding a wealth of information about the elementary, atomic-scale mechanisms of solidification and crystallization. We note, however, that such atomistic simulations of growth processes are difficult due to system size, physical time span, and intensive computational requirements, which typically limit the spatial extent of the simulated systems to several nanometers (i.e., simulations of the dynamics of several thousand atoms, with appropriate periodic boundary conditions) and the physical time span to up to about a nanosecond. These considerations guide the design and assessment of the simulations and lead to judicious choices of the phenomena to be investigated.

In this paper we focus on epitaxial growth of amorphous-silicon (*a*-Si) films from the vapor, which is one of the most commonly used methods for the preparation of thin films of amorphous materials. Main issues in studies of amorphous semiconductors (and other amorphous materials) include the structural characterization of these materials, the correlation between the structure and the properties of the materials, and the dependencies of the above on the method of preparation.[27] Such dependencies of the growth mode, and consequently, of variations in the physical properties of amorphous solids with the conditions of formation, have often been observed[28] and may arise from structural changes on various length scales (such as local variations in network structure, a distribution of voids,[29–36] columnar morphologies,[7,37–45] and other microstructural effects).

The structure, dynamics, and energetics of bulk amorphous silicon have been investigated previously via MD simulations, where several schemes for quenching from the melt have been employed.[46–52,9,10] In a most recent study,[10,52] we have shown that, using the Stillinger-Weber Si potentials,[53] it is possible to prepare amorphous silicon via *direct* cooling of the melt, and that the structural and dynamical properties of the sample so generated are in good agreement with available experimental data for the static structure factor and vibrational density of states. Furthermore, this study provided evidence for a lack of medium-range order, measured via correlations between dihedral angles associated with adjacent bonds.

We note, however, that, in practice, the most often used method for preparing amorphous silicon (and other amorphous semiconductors) is by growth via deposition from the vapor phase, and that the presence of voids and other inhomogeneities (on a wide spectrum of length scales) is a common feature in these systems. The characteristics of the void distribution have been shown experimentally to depend on growth conditions, and it is believed that such structural inhomogeneities result in the density of elemental amorphous semiconductors (silicon and germanium) being lower than their corresponding crystalline phases. Recent MD studies,[54] in which voids of various sizes have been introduced into bulk amorphous silicon, have shown that theoretical amorphous-silicon models, generated via MD simulations and employing recently developed interaction potentials which include two- and three-body interactions, can describe the intense small-angle scattering observed experimentally[30–36] [i.e., the Guinier relation,[55] where the presence of voids results in a rapid increase of the static structure factor $S(k)$, for $k < 1$ Å^{-1}]. Furthermore, these studies show that the presence of voids decreases the local strain in the *a*-Si network.

Other microstructural features, which are often observed in amorphous systems using a variety of techniques[1–7] (microfractography, transmission electron microscopy, and small-angle electron and x-ray scattering), are columnar growth morphologies and tubular, or pipelike, voids. The columnar structure consists of close-to-parallel rod-shaped regions of high density that are surrounded by a material tissue of lower density. The origin of columnar structures in most thin-film deposition processes is related to shadowing of the intercolumnar regions from a directional flux of incident particles.[7] The initiation of this growth mode has been connected to initial roughness in the substrate and self-shadowing due to fluctuations in the topography of the growing film. Thus the development of these structures may be described as a topographical inhomogeneity (either present in the substrate or dynamically developed during growth) which is perpetuated by the smaller collecting angles for incident particles in the intercolumnar regions ("valleys") than for sites on the tops of the high-density regions ("hills").

Early computer simulations of columnar growth focused on the geometrical aspects of the problem,[7,39(b),56] employing hard spheres (or two-dimensional hard disks) and limited-mobility deposition schemes, resulting in apparent confirmations of the empirical geometrical relationship between the polar angle of incidence of the impinging beam, θ, and the angle, ϕ, between the columnar grains and the substrate normal, $\tan(\theta)=2\tan(\phi)$, referred to as the "tangent rule".[7,38] However, more recent MD simulations[7] (employing Lennard-Jones interaction potentials), and certain ballistic deposition models,[57–59] have demonstrated, in agreement with experimental observations,[40,60–62] the nonunique relationship between ϕ and θ, and, in particular, the dependence of ϕ on deposition conditions, such as substrate temperature, deposition rate, angle of incidence, and surface mobility. In general,[7] it is observed that the tendency for columnar growth is enhanced by factors which limit the mobility of the deposited particles (e.g., for high-melting-point elements, for compound and elemental materials of high binding energy, and for deposition at low temperatures).

The focus of previous[23,24,26] MD simulations of vapor-phase-epitaxial growth of silicon has been on determining the conditions which are optimal for growth of ordered crystals. In contrast to the growth of materials characterized by spherically symmetric interatomic interaction potentials (such as metals), these simulations have shown that, in the case of silicon, epitaxial growth into a properly stacked, ordered crystalline film occurs at high substrate temperatures, T_s, while at low T_s an amorphous film is grown. The focus of our investigations, on the other hand, is on the dynamics and mechanisms of growth of amorphous-silicon films and on identification of certain deposition parameters (such as incidence geometry) which control the growth mode and the structural characteristics of the grown film. In addition, we provide information about the structure of the interfacial region between the crystalline substrate and the epitaxially grown *a*-Si film.

The simulation method and other pertinent technical details are given in Sec. II. Results and analyses of simulations of thin *a*-Si films grown under several conditions, exhibiting uniform film growth for normal incidence, preferential orientation of density inhomogeneity corresponding to columnar growth for an incident beam directed at 60° from the surface normal, and the formation of voids for deposition using random incidence directions, are presented in Sec. III. A summary of our observations is given in Sec. IV.

II. METHOD

In our studies we have simulated, using the MD technique, the epitaxial growth from the vapor of *a*-Si films, deposited onto (111) crystalline-Si substrates. In these simulations the initial calculational cell consists of two static crystalline-Si layers and three dynamic crystalline layers which are positioned on top of the static substrate, exposing the (111) surface. The directions in the plane of the calculational cell are $[1\bar{1}0]$ and $[10\bar{1}]$, with the outward normal in the [111] (Z) direction. The number of atoms in each of the crystalline layers in N_l, and while two-dimensional periodic boundary conditions are imposed in the directions parallel to the surface plane, the system is free in the Z ([111]) direction.

To simulate the growth process, following equilibration of the crystalline substrate at room temperature ($T = 300$ K), particles are released at a rate of one particle every N_r integration time steps, Δt (where $\Delta t = 1.15 \times 10^{-3}$ psec is the intergration time step), from a randomly chosen position on a planar source located above the substrate outside the range of interatomic interactions. Whenever an atom to be released is created (at a random location on the planar source), such that it is within the interaction range of any previously released atom, it is discarded and a new random choice of a point of release on the planar source is generated. By this procedure we avoid undesirable sudden acceleration of beam atoms near the source. By monitoring the frequency of such events, we found that they are rare and randomly distributed in time. Consequently, no correlations develop between the release positions of the deposited atoms from the source. In addition, atoms which, due to interactions with other beam particles, drift upwards past the source, are discarded. The initial kinetic energy of the deposited particles is set to $3k_B T_{cm}/2$, where T_{cm} is the melting temperature of crystalline Si ($T_{cm} = 1665$ K for the Stillinger-Weber potential[18,19] compared to the experimental value of 1683 K) and is equivalent to 0.145 eV, and their incidence direction is chosen according to the objective of the simulation.

Amorphous-silicon film growth was simulated for three incidence geometries: (i) incidence along the normal (Z) to the surface, with $N_l = 49$ atoms per crystalline substrate layer, and a release rate of one particle every $N_r = 500$; (ii) incidence along a direction inclined by 60° from the surface normal, with the plane of incidence defined by the [111] and $[1\bar{2}1]$ directions with $N_l = 96$ and $N_r = 250$ (thus yielding the same flux as in the other incidence geometries); and (iii) random incidence, such that the azimuthal angle of the velocity vector of each released particle is chosen randomly in the range $(0, 2\pi)$ and $\cos^2\theta$ of the polar angles, θ, between the particles' initial velocities and the normal to the surface is distributed uniformly between 0 and 1. In these simulations, $N_l = 49$ and $N_r = 500$.

In our simulations we have used the interaction potentials developed by Stillinger and Weber[53] (SW), which include two- and three-body contributions (V_2 and V_3, respectively), and which have been used extensively in studies of crystalline solid and liquid bulk[53] and surface[63] phenomena of silicon, in investigations of amorphous Si,[46,48,49,52,54,64] [and a-Ge (Ref. 47)], and in studies of the structure and dynamics of equilibrium[19,65] and nonequilibrium[18] (liquid-phase-epitaxy) solid-melt interfaces of Si. The energy scale which we use is $\varepsilon = 50$ kcal/mol, the length scale $\sigma = 2.0951$ Å, and the time unit, t.u. is 7.66×10^{-14} sec [temperature is expressed in units of ε; to convert to degrees kelvin multiply by $(2.5173 \times 10^4$ K$)/\varepsilon$]. In this unit the melting temperature of crystalline silicon (T_{cm}) is 0.0662 and that of bulk a-Si (Ref. 52) $T_{am} \simeq 0.04$. The classical Newtonian equations of motion were integrated using Gear's fifth-order predictor-corrector algorithm using a time step $\Delta t = 0.015$ t.u.$= 1.15 \times 10^{-3}$ psec.

The temperature of the system was controlled via scaling of particles' velocities. In our preliminary studies the velocities of particles in only the first layer of the dynamic crystalline substrate adjacent to the static substrate were scaled to one-tenth of room temperature. However, we have found (see Sec. III) that, as atoms are continuously deposited and the thickness of the amorphous film increases, the removal of heat from the system through the substrate becomes inefficient, and that the interfacial region at the growth front of the film heats up to above the a-Si melting point. In fact, Biswas *et al.*[26] have recently analyzed this issue and have concluded that in a previous[23] MD study of epitaxial growth of silicon, where heat was removed via scaling of velocities in a similar manner, the entire deposited growth front had melted and consequently the growth process observed[23] was that of a solid growing into a liquid rather than MBE-type growth. To avoid this problem, which in our simulations developed only for the normal- and random-incidence deposition geometries where very thick films were grown, we have adopted a scheme where the velocities of all particles in the system, *except* for the N_p most recently deposited particles, are scaled to bring the *average temperature* of the system to room temperature every 10 integration time steps (Δt), throughout the simulation ($N_p = 8$ and 32 for the normal- and random-incidence simulations, respectively). In applying the temperature control, the factor by which the velocities of the $N - N_p$ atoms are uniformly scaled (where N is the number of dynamic particles in the system at the time that the temperature control is applied) is given by $s = (T_0/T)^{1/2}$, where the desired temperature $T_0 = 300$ K and

$$T = \frac{2}{3(N - N_p)} \left\langle \sum_{i=1}^{N-N_p} \frac{mV_i^2}{2} \right\rangle , \tag{1}$$

where the angular brackets denote averaging over the 10-time-step interval between temperature rescalings. Thus the temperature rescaling is determined by the average temperature of the whole system. Since the number of particles in the bulk of the film is large compared to that in the vicinity of the growth interface, the modification to the velocity of any given atom is very small (typically $s = 0.999$). In particular, over the time period that it takes for heat generated by a deposited particle to dissipate from the impact region to the underlying grown film via natural diffusion processes (see Sec. III A), the dynamics of particles at the interface region is only slightly modified, and thus the mobility of the deposited atoms just after impact is not altered significantly. The values of N_p were chosen to allow adequate dynamical evolution of the deposited beam atoms before they are included in the list of temperature-controlled particles. Thus, time is allowed for the natural development of energy pathways and dissipation mechanisms of the heat generated by the deposition and growth processes, while maintaining the major portion of the system, and, in particular, the surface region, below the melting temperature of *a*-Si.

The required rate of heat dissipation is also related to the deposition flux. The flux of incident particles which we used (~ 2.8 atoms/nsec Å^2) is comparable to those used in previous simulations.[23,26] While still higher than deposition fluxes used experimentally (which cannot be simulated due to prohibitive computational constraints), through the combination of the flux of deposited beam particles and the heat-removal procedure employed in our simulations, we have attempted to model and faithfully simulate the main mechanisms and structural features of *a*-Si film growth.

III. RESULTS

Prior to presenting our results for epitaxial growth of *a*-Si films for the various incidence geometries, we address the issue of heat dissipation during deposition and growth and its influence on the film-growth process.

In Fig. 1 plots of particles' trajectories, viewed along the $[10\bar{1}]$ direction, for a system generated by normal-incidence deposition with heat removal via cooling of the bottom layer of the underlying dynamical crystalline substrate to one-tenth of room temperature, are shown, for two stages of the simulation [Fig. 1(a) for an earlier stage, 1(b) for a later one]. In addition, profiles along the Z direction of the particle density, kinetic temperature, three-body potential energy per particle, and average coordination number are shown in Figs. 2(a)–2(d) and 2(e)–2(h) for the two growth stages, respectively. We observe that while at the earlier growth stage [Fig. 2(b)] the temperature T in the vicinity of the growth front is well below the *a*-Si melting temperature, T_{am} (which we determined previously[52] to be $\sim 0.04\varepsilon$), the temperature in this region increased, approaching T_{am}, at a latter stage of the growth process [see Fig. 2(f)]. Upon continued growth, the top region of the film will melt. The spike in the temperature near the growth-front interface corresponds to the increase in the kinetic energy of an impinging particle as it accelerates due to its interaction with atoms at the top of the film.

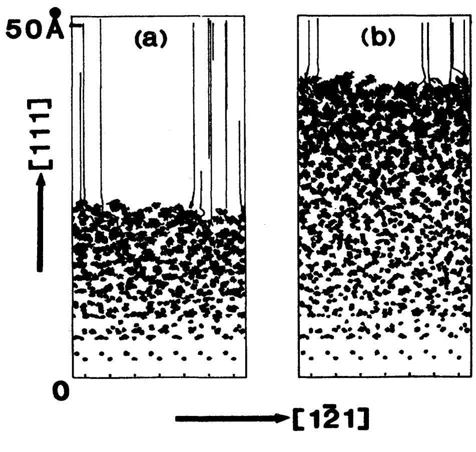

FIG. 1. Particle trajectories viewed throughout the system along the $[10\bar{1}]$ direction (see inset in Fig. 8 for definition of directions) for a thin *a*-Si grown by normal-incidence deposition onto a Si(111) substrate (bottom three layers), with heat removed via scaling of particles' velocities at the bottom dynamical substrate layer to one-tenth of room temperature. The linear dimension of the system along the $[1\bar{2}1]$ direction is 23.27 Å. Views at (a) an early stage of the simulation and (b) at a later one are shown. Comparison of trajectories at the top of the grown *a*-Si film demonstrate the enhanced mobility of particles in this region at the later stage, (b), due to heating.

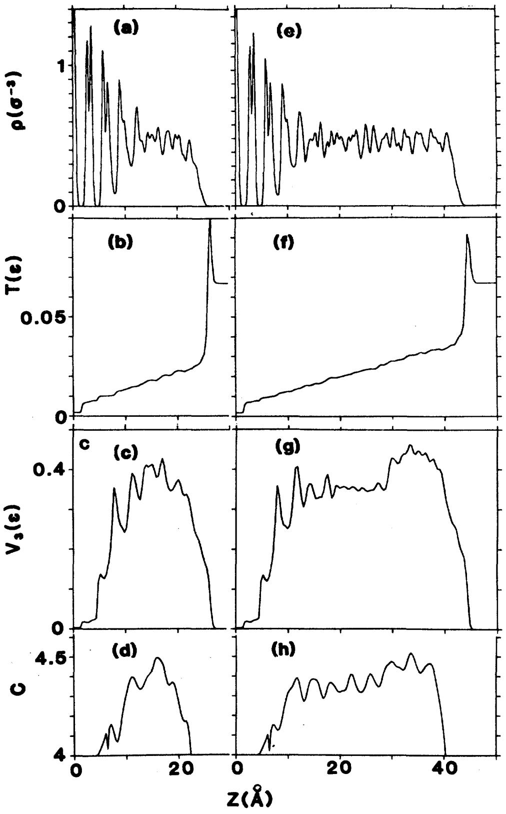

FIG. 2. Profiles along the Z ([111]) direction, normal to the substrate surface, of the density (ρ), kinetic temperature (T), three-body contribution to the potential energy (V_3), and coordination number (C), for the system described in Fig. 1. The profiles in (a)–(d) were taken at the end of the early stage in the growth simulation [see Fig. 1(a)], and the ones in (e)–(h) correspond to the end of the later stage [see Fig. 1(b)]. Note the increase in temperature at the surface of the film at the later stage of growth [compare (b) and (f)], approaching the *a*-Si melting point ($T_{am} \simeq 0.04$). This increase is accompanied by an increase in V_3 at the surface region of the thicker film, (g), as well as an increase in coordination number, which indicate that the material at the top part of the film is characterized by a smaller degree of tetrahedral bonding akin to glassy (or liquidlike) order. Density in units of σ^{-3}, $\sigma = 2.0951$ Å; energy and temperature in units of $\varepsilon = 50$ kcal/mol.

Accompanying the increase in temperature, the nature of the interfacial region near the growth front is changed (i.e., in the later stage it is liquidlike), resulting in enhanced mobility of the deposited particles at the interface [compare particle trajectories in Figs. 1(a) and 1(b)], which alters the kinetics of the solidification process, yielding in this region a film characterized by a higher value of the three-body–potential contribution (V_3), and a higher overall coordination number of the atoms [compare Figs. 2(c) and 2(d) with Figs. 2(g) and 2(h)]. Note that V_3, which by construction represents the covalent tetrahedral bonding in Si, approaches zero for an ideally tetrahedrally coordinated crystal, and that deviations from tetrahedral bonding are exhibited by positive values of V_3. We note that the properties of the material at the top part of the sample at the later growth stage are more akin to those of supercooled Si liquid or silicon glass[49] than to a-Si. Finally, we remark, that as long as the temperature near the surface of the film is well below T_{am} [see Fig. 2(b)], the properties of the grown film are similar to those of a film of similar thickness whose growth was simulated using our modified heat-removal procedure (see subsection A).

In view of the above observations, which demonstrate the deterioration during growth of the efficiency of heat removal from the deposited film, we have adopted the temperature-control procedure described in Sec. II.

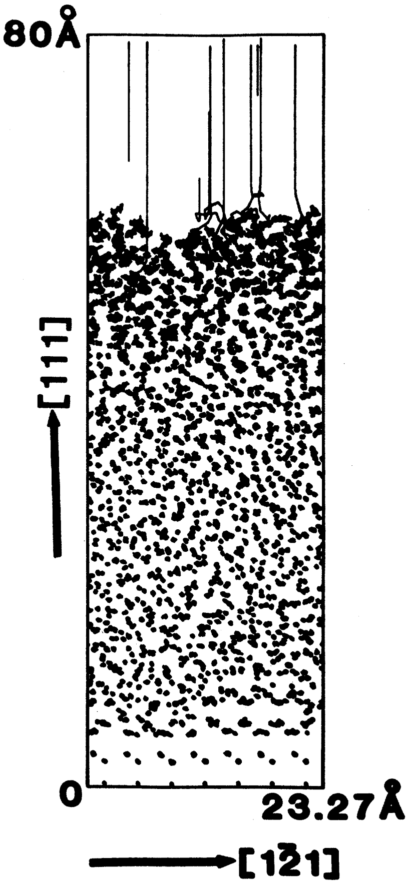

FIG. 3. Particle trajectories at the end of the simulation of a-Si epitaxial growth with particles incident along the normal, [111], direction. The system is viewed along the [10$\bar{1}$] direction. The temperature of the system was controlled according to the modified procedure described in the text.

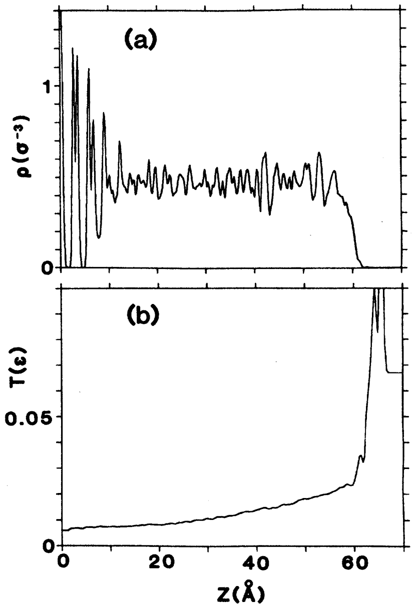

FIG. 4. Profiles of the density and temperature along the Z ([111]) direction toward the end of the simulation of a-Si epitaxial growth using a normal incident beam. Note that even though the thickness of the grown film is larger than that described in Figs. 1(b) and 2(e)–2(h), the temperature at the top of the film is well below T_{am}, as a result of the more efficient heat-removal procedure adopted in this simulation. The large temperature spikes for $Z > 60$ Å [in (b)] correspond to accelerated incident particles. Density in units of σ^{-3}, $\sigma = 2.0951$ Å, and temperature in units of $\varepsilon = 50$ kcal/mol.

A. Normal incidence

Particle trajectories and profiles of the density, and temperature, near the end of the simulation, for the a-Si film grown under normal-incidence conditions, are shown in Figs. 3 and 4, respectively. As seen from Fig. 4(b), employing our method of heat removal, the temperature remains well below T_{am} throughout the film. Moreover, detailed examination reveals that the grown film exhibits structural and energetic properties which are uniform throughout the system (for structural characteristics of the system, cooled after the termination of the growth simulation to 300 K, see Table I), except at the region at the interface between the dynamic crystalline Si(111) substrate and the grown a-Si film. From the density profile [Fig. 4(a)], we observe that the material in this interfacial region ($5 \le Z \lesssim 12$ Å) exhibits a certain degree of order in the direction normal to the (111) substrate [first three peaks, from the left in Fig. 4(a), i.e., $Z < 5$ Å] extending over a distance equivalent to about three crystalline Si(111) double layers. An expanded view of the density profile in this region is shown in Fig. 5(a), and particle trajectories in a slice through the system as shown in Fig. 6. We note that while the interface between the crystal-

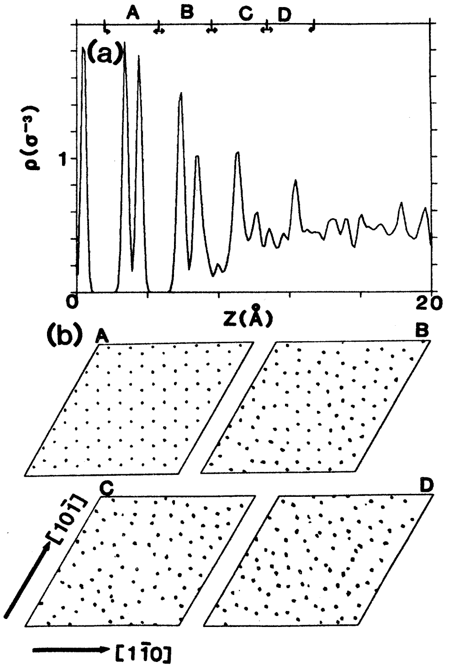

FIG. 5. (a) Expanded view of the density profile shown in Fig. 4(a) in the range $0 \leq Z \leq 20$ Å. (b) Particle trajectories in regions $A-D$ [see top of (a)], viewed down the [111] direction, i.e., normal to the substrate surface plane. Region A corresponds to the top two layers of the dynamic crystalline Si(111) substrate. $B-D$ correspond to the interfacial region of the deposited a-Si film. Note the partial crystalline order in regions B and C, which corresponds to the crystalline-like features in the density profile, in these interfacial regions [see (a)].

line substrate and the grown film exhibits a layered structure, the deposited film in this region possesses structural properties which are only of partial crystalline character, as may be seen from the particle trajectories in slices through the system viewed along the [111] direction shown in Fig. 5(b). In Fig. 5(b) the slices marked $A-D$ correspond to the regions marked, respectively, in Fig. 5(a). Region A encompasses the top two layers of the dynamic crystalline substrate, and regions $B-D$ comprise the interfacial region of the grown film. The trajectories shown in Fig. 5(b) (and Fig. 6) reveal that the partial order in this interface originates from crystalline intrusions embedded in an amorphous environment. This interfacial structure is different from that occurring at the interface between a solid and a liquid (both at equilibrium[13,15–17,19,64–70] and under growth conditions[15–18]), which has been documented previously and which can be described using liquid-state theories with properly chosen boundary conditions.[66–68] Unlike the case of liquid layering at *flat* Si solid-liquid interfaces [such as the crystalline-to-melt interface at the Si(111) surface[19,65]], where the degree of order in the stratified interfacial region is uniform parallel to the solid surface plane, the structural characteristics of the interfacial films grown by epitaxy from the vapor are nonuniform parallel to the crystalline substrate, exhibiting over a region of ~8 Å partial crystalline and amorphous character.

The rough morphology at the top of the grown film (see, e.g., Fig. 6) is typical of that observed throughout the entire growth process. While for random-incidence deposition (see subsection C) such surface inhomogeneities can lead to the formation of voids, such microstructure does not develop at normal-incidence deposition, resulting in a more uniform density distribution in the grown film.

To elucidate the mechanisms of growth, we show in Fig. 7 plots of the time evolution of the kinetic temperature, per particle potential energy (in units of $\varepsilon = 50$ kcal/mol), and of a measure of the particles' mobility, $R_i^2(t) = [(\mathbf{R}_i(t) - \mathbf{R}_i(t_0)]^2$, for the deposited particles (these results are averaged over the trajectories of 40 deposited particles toward the end of the simulation). The time origin, $t_0 = 0$, in these plots is the instant when the deposited particle first experiences an interaction with the substrate atoms. We observe [Fig. 7(d)] that initially the kinetic energy (temperature) of the deposited particles

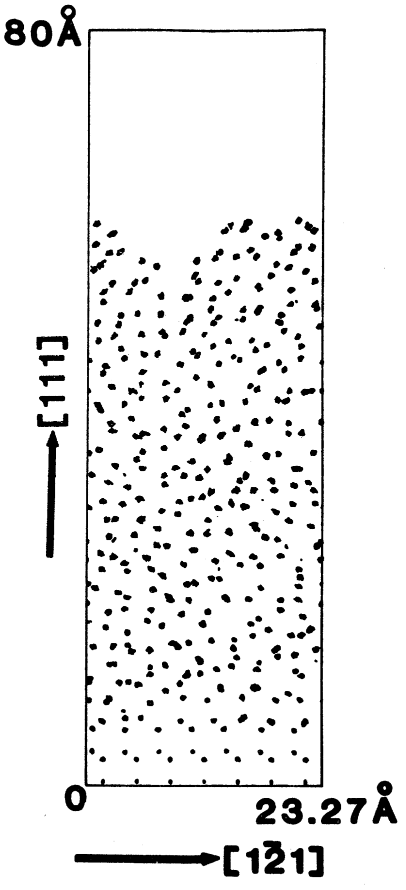

FIG. 6. 5-Å slice through the system, viewed along the [101̄] direction, demonstrating the partial crystalline order at the interface between the crystalline dynamic substrate (bottom three layers) and the deposited a-Si film (compare to Fig. 5).

increases due to the acceleration resulting from their interaction with the substrate and the bonding to it. Subsequently, this kinetic energy is dissipated, in an efficient manner, to the rest of the system, over a short time span of about 2 psec (i.e., ~1700 integration time steps). This observation guided us in constructing the thermalization procedure described in Sec. II. We remark that we obtained similar results from simulations where heat was removed via scaling of particle velocities in the first dynamic layer only (as long as the thickness of the grown film was not too large). Furthermore, the properties of an amorphous film grown via normal-incidence deposition of particles whose initial kinetic energy was one-third of the beam energy used in the simulations described here were found to be essentially the same as those of the film grown via normal incidence of the higher-energy beam. These results further substantiate our conclusion that the mobility of the deposited atoms and the dynamics of particles in the impact region are not significantly influenced by our more efficient thermalization procedure. These results, which are in contrast to the much slower rate of energy dissipation for low-energy Si atoms impinging upon a *smooth crystalline surface*,[26] demonstrate the efficient damping of the particles' kinetic energy upon incidence on *amorphous or disordered substrates* due to the lack of order in the surface which enhances collisional energy transfer rates. Furthermore, the $R^2(t)$ plot versus time, shown in Fig. 7(a), and its components parallel $[R_{\parallel}^2(t)]$ and normal $[R_{\perp}^2(t)]$ to the (111) surface, shown in Figs. 7(b) and 7(c), respectively, indicate the limited mobility of the deposited particles on the surface. Most of the initial rise in $R^2(t)$ is due to the distance traveled by the deposited particle from its location at t_0 (i.e., first instance of interaction with the substrate) to the bonding site. The lack of any significant particle diffusion at the surface correlates with the observation that growth via vapor-phase epitaxy of crystalline films of tetrahedrally bonded materials requires relatively high substrate temperatures, while growth at low substrate temperature yields a disordered film, in contrast to the results found for other materials (such as metals) where the reverse occurs. The origin of the difference is in the relatively strong local bonding characteristic of covalent materials, and, consequently, high-potential-energy barriers for particle diffusion. Finally, we note the continued slow decrease of the particle potential energy [see Fig. 7(e)] as the particles explore their local-bonding environment, which itself changes as additional beam atoms are deposited.

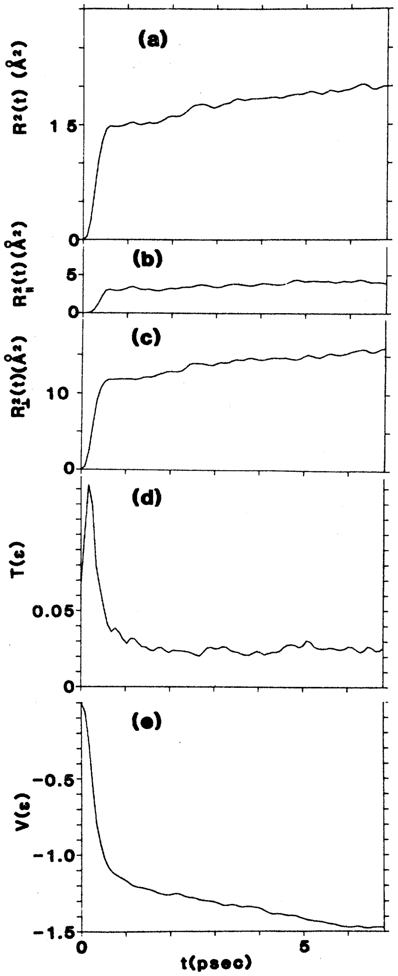

FIG. 7. Time evolution of $R^2(t)$ and its components parallel $[R_{\parallel}^2(t)]$ and perpendicular $[R_{\perp}^2(t)]$ to the (111) surface plane, and of the kinetic temperature T and per-particle potential energy V. These quantities are calculated for individual incident particles, with the time origin taken for each particle as the instant when the deposited particle first experiences an interaction with the substrate film atoms. The results shown are averaged over the trajectories of 40 incident particles, toward the end of the normal-beam MBE simulation. Note the fast rate of kinetic-energy dissipation [in (d)] following the initial increase due to acceleration of the incident particle towards the surface. The results in (a)–(c) demonstrate the lack of significant diffusion on the surface. Energy and temperature in units of $\varepsilon = 50$ kcal/mol, time in psec, and distance in Å.

Results similar to those shown in Fig. 7 were obtained for the other incidence geometries, which we now discuss.

B. Oblique incidence

To investigate the dependence of the morphology of the grown film on the angle of incidence of the deposited particles, we have performed simulations in which a beam of low-energy (initial kinetic energy equals $3k_B T_{cm}/2$, where T_{cm} is the crystalline melting temperature) silicon atoms impinges upon a Si(111) crystalline, room-temperature substrate, and the initial velocities of the particles are directed at 60° from the normal to the (111) surface, with the plane of incidence defined by the [111] and $[1\bar{2}1]$ directions (see inset of Fig. 8).

Particle trajectories of the system toward the end of the simulation are shown in Fig. 8. In Fig. 8(a) a view along the $[10\bar{1}]$ direction through the whole calculational cell is shown. The microstructure in the grown film is revealed in Figs. 8(b) and 8(c), where a view of the system from above (along the [111] direction and excluding the crystalline substrate, in Fig. 8(b)) and a slice through the

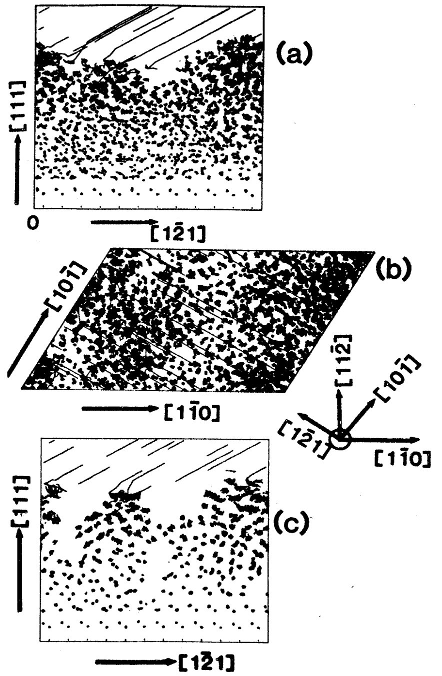

FIG. 8. Particle trajectories for MBE growth using a beam directed at 60° from the normal to the Si(111) substrate, taken towards the end of the simulation. (a) View of the whole system along the $[10\bar{1}]$ direction. (b) View of the whole system (excluding the crystalline substrate) from above (along the [111] direction), exhibiting regions of higher and lower densities. (c) View along the $[10\bar{1}]$ direction of a slice of the system, with the cutting plane defined by the [111] and $[1\bar{1}0]$ directions, and containing the lower portion of the plane shown in (b), demonstrating the columnar microstructure. The dimension of the system along the $[1\bar{2}1]$ direction is 39.9 Å.

system [Fig. 8(c)], with the cutting plane defined by the [111] and $[1\bar{1}0]$ directions, containing the lower portion of the plane shown in Fig. 8(b) and viewed along the $[\bar{1}01]$ direction, exhibit regions of higher and lower density corresponding to a columnar microstructure in the film.

Stages in the growth of the film, exhibiting the development of the columnar microstructure, are shown in Fig. 9, where a sequence of particle trajectories in a slice through the system [the same as that shown in Fig. 8(c)] is given. (In this figure the calculational-cell length along the $[1\bar{2}1]$ direction is duplicated for visual impression.) In each of the panels of Fig. 9, trajectories for a time span of 6.9 psec (i.e., $6000\Delta t$) are shown. The first frame [Fig. 9(a)] starts at $t=0$ psec (i.e., the beginning of the simulation), and the interval between successive frames is 57 psec. As seen from Figs. 9(a)–9(c), the initial stage of growth involves a stochastic nucleation of two-dimensional islands on the substrate which provide the nuclei for the growth of there-dimensional clusters in a process which involves deflections of the trajectories of impinging particles. Further growth of these clusters shadows the intercluster regions, and a film characterized by preferentially oriented density inhomogeneities, corresponding to a columnar microstructure, develops [see Figs. 9(d)–9(h)]. We note the marked crystalline structure at the bases of the columns. Detailed inspection of the trajectories of deposited particles reveals that the factors underlying the growth of this structure are of geometrical (angle of incidence of the beam) and dynamical interaction origins (i.e., deflection of impinging particles' trajectories due to interactions with film atoms).

Columnar structures, i.e., preferential orientation of density inhomogeneities, in amorphous films occur on various length scales. Our discussion is limited by the nature of our simulations to microstructures, i.e., structural characteristics of microscopic (tens of angstroms) dimensions. In this context we remark that, in view of the mechanism of the development of the observed microstructure, which, as discussed above, involves in the initial stages small localized islands and clusters from which the microstructure evolves via shadowing of the intercluster valleys, we conclude that for the conditions of our simulations the geometrical characteristics of the simulated microstructure (and their analysis; see below) are not influenced in a significant manner by size effects or the two-dimensional periodic boundary conditions imposed in the directions parallel to the surface plane.

Characterization of the microstructure can be given in terms of the spatial extents and orientations of the densi-

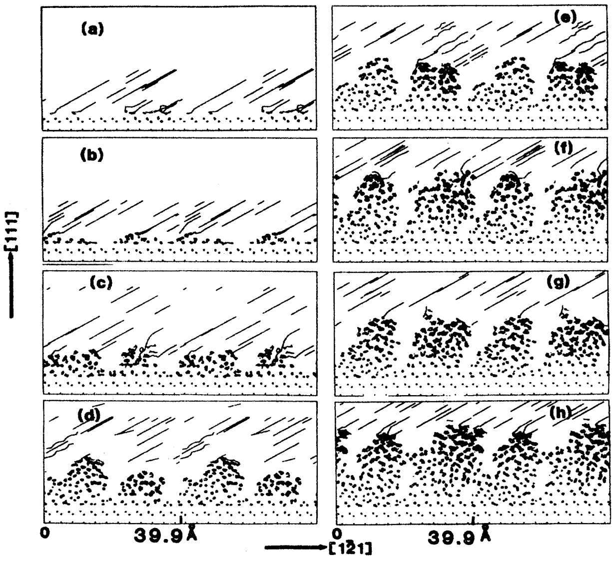

FIG. 9. Evolution of the microcolumnar structure in MBE on a Si(111) substrate, using a beam directed at 60° from the normal to the surface. In each of the frames trajectories for a time span of 6.9 psec are shown, and the interval between successive frames is 57 psec. The view is along the $[10\bar{1}]$ direction. (a) Nucleation of two-dimensional crystalline islands. (b) and (c) Growth of three-dimensional clusters. (d)–(h) Growth of columnar microstructure, and the development of intercolumnar voids due to shadowing and deflection of incident particles' trajectories. The length of the calculational cell along the $[1\bar{2}1]$ direction is 39.9 A, and it was duplicated along this direction for visual impression.

ty inhomogeneities in the system. To quantify the distribution of angles, ϕ, that the low-density regions, i.e., intercolumnar voids (and, in turn, the columns), make with respect to the normal to the substrate, various measures can be developed. To obtain such a measure, we partition the calculational cell into a series of thin parallelepiped slabs (bins) whose base is in the plane of the surface (i.e., defined by the $[1\bar{1}0]$ and $[10\bar{1}]$ directions), and whose third axis is oriented at a specified angle ϕ with respect to the [111] direction. Each slab is a thin slice of the $[1\bar{1}0]$ (X) direction whose width extends across the whole calculational cell in the $[10\bar{1}]$ direction. We then count the number of atoms in each of the bins and form a measure of the bins' occupancies. The summation of this measure over all the bins, repeated for a range of angles, ϕ, yields a "column-orientation distribution function" (CODF), $P(\phi)$. By construction, the CODF provides an objective global-statistical measure of the orientational distribution of density inhomogeneities in the material and does not assume, nor is it predicated on, the existence of any number of columns. The occupancy measures we consider below are constructed to accentuate the density-deficient regions in the system, and their orientational distribution, which, in turn, coincides with the orientational distribution of the adjacent high-density ("columnar") regions.

There are many possibilities for an occupancy measure. For example, to within a normalization factor, Sikkens[3(b)] uses

$$\sum_{i=1}^{N_b}[N_i(\phi)-\bar{N}]^2 \tag{2}$$

as a CODF, where $N_i(\phi)$ is the number of atoms found in the ith bin for inclination angle ϕ, N_b is the number of bins, and $\bar{N}$ is the expected number of atoms in the bin for a uniform distribution of the atoms in the system. The above CODF peaks for those angles for which the low-density regions, i.e., intercolumnar voids, extend for appreciable distances, thereby leading to large values of the measures for the bins at those angles.

Since our system is comprised of a thin film, the bins extend between fixed limits along the Z ([111]) direction, and are of the same volume for all orientations, ϕ. In our calculations we take as the lower Z axis limit a value of 3.75 Å above the topmost dynamic crystalline layer, in order to lessen the effect of the substrate crystalline symmetry on our CODF. For the maximum Z-axis limit we take the value at the top of the grown film. We have used 20 bins along the $[1\bar{1}0]$ axis and averaged over three choices of bin origins along this axis.

We have considered two alternative choices for $P(\phi)$:

$$\sum_{i=1}^{N_b}[N_i(\phi)-\bar{N}]^2 \tag{3}$$

and

$$\sum_{i=1}^{N_b}\exp[-\lambda N_i(\phi)/\bar{N}]\ , \tag{4}$$

where λ is a constant. In each case we normalize $P(\phi)$ by the requirement that, when summed over all angles ϕ, $\sum P(\phi)=1$. For $\lambda=1$ both choices of $P(\phi)$ yield very similar results, as seen from Figs. 10(a) and 10(b), exhibiting several peaks. Since the film grown in our simulations is relatively thin, roughness at the top surface of the film makes a large, undesirable, contribution to $P(\phi)$. In order to minimize these surface effects and accentuate the presence of low-density regions, i.e., intercolumnar voids that extend deep into the film, we increase the value of λ in our second choice for $P(\phi)$, thus increasing the relative contribution from those bins that encompass the most density-deficient regions in the film. The result for the second choice for $P(\phi)$ with $\lambda=10$ is shown in Fig. 10(c). The dominant peak in this figure corresponds to intercolumnar voids, inclined at an angle ϕ of ~41° with respect to the normal, in agreement with the value predicted by the tangent rule [$2\tan(41°)=1.738\simeq\tan(60°)$].

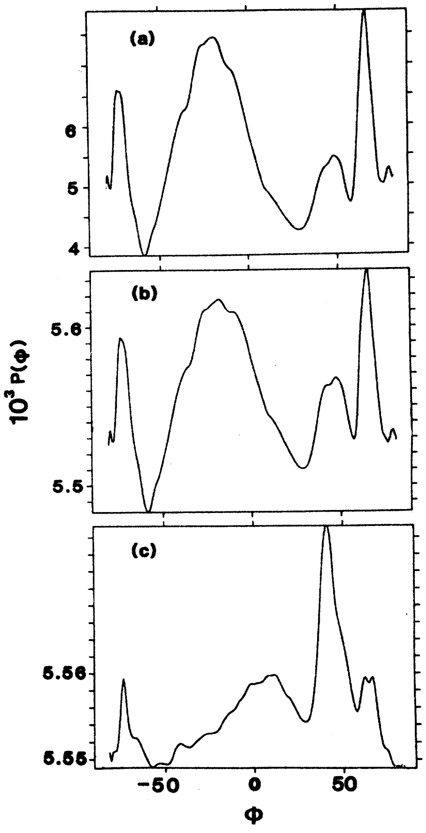

FIG. 10. Plots of column-orientation distribution functions (CODF's), $P(\phi)$. (a) $P(\phi)\propto\sum_{i=1}^{N_b}[N_i(\phi)-\bar{N}]^2$, suggested by Sikkens *et al.* [Ref. 3(b)]. (b) $P(\phi)\propto\sum_{i=1}^{N_b}\exp[-\lambda N_i(\phi)/\bar{N}]$ for $\lambda=1$. (c) Same as (b), but $\lambda=10$. In each case $P(\phi)$ is normalized by the requirement $\sum P(\phi)=1$, where the sum is over all the angles ϕ. The CODF in (c) accentuates the contribution from intercolumnar voids that extend deep into the film. From (c) we determine that the intercolumnar voids are inclined at an angle of 41° with respect to the normal to the surface, in agreement with the value predicted by the tangent rule.

C. Random incidence

Having discovered that deposition in the normal-incidence geometry yields a uniform *a*-Si film and that deposition with a beam directed at 60° to the surface normal results in a columnar microstructure, we turn next to *a*-Si film growth under a random-angle deposition geometry. As described in Sec. II in these simulations the particles were released from the planar source with the azimuthal angle of their initial velocity uniformly distributed between 0 and 2π and with $\cos^2\theta$ of the polar angles, θ, between the particles' initial velocities and the surface normal, distributed uniformly between 0 and 1. A time sequence of particles' trajectories in 5-Å-thick slices through the system (with the cutting plane defined by the [111] and [$1\bar{1}0$] directions and viewed along the [$10\bar{1}$] direction) is shown in Fig. 11. Profiles along the Z axis ([111] direction) for the system (cooled to room temperature at the end of the growth process), of particle density, temperature, potential energy, and the fraction of four and fivefold coordinations, are given in Fig. 12.

As is evident from Fig, 11(b), the density distribution, toward the end of the simulation (1069 psec after the start of the simulation), in the grown amorphous film is nonuniform, exhibiting regions of marked density deficit, i.e., voids. The time sequence of trajectories shown in Figs. 11(a)–11(h) is such that in each frame trajectories for a time span of 6.9 psec are shown, starting in Fig. 11(a) at $t=333$ psec after the beginning of the simulation, and the time interval between successive frames is 115 psec (remember that a particle is released from the source every 0.575 psec). We observe that the mechanism of for-

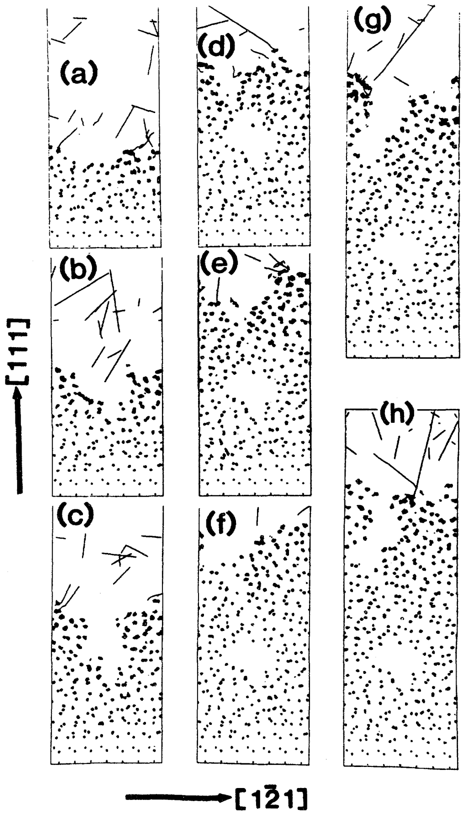

FIG. 11. Stages in the evolution of voids in an *a*-Si film grown via deposition from the vapor, with the incident particles released from the planar source at random directions with respect to the surface normal. Particle trajectories are viewed along the [$10\bar{1}$] direction for a 5-Å-thick slice through the system, with the cutting plane defined by the [111] and [$1\bar{1}0$] directions. The time span in each frame is 6.9 psec, and the interval between successive frames is 115 psec, with the first frame, (a) starting at 333 psec after the beginning of the simulation. Note the development of a void in (a)–(c), which is then capped off, (d), and the development of a second void, (e)–(h). Length along the [$1\bar{2}1$] is 23.27 Å.

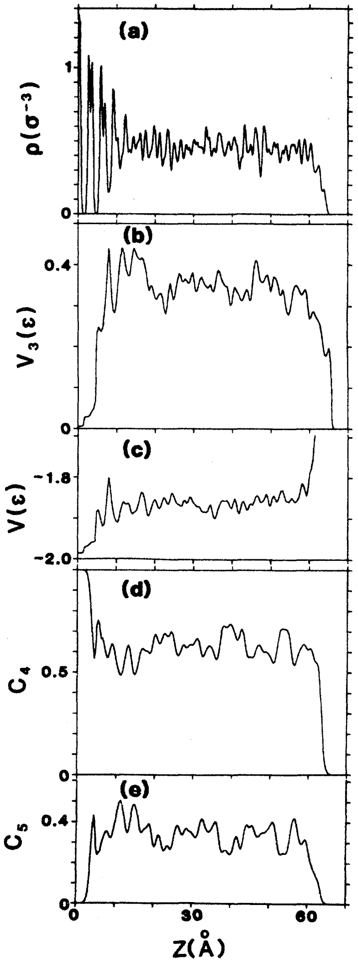

FIG. 12. Profiles along the Z direction of the density (ρ), of the per-particle three-body contribution to the potential energy (V_3) and the potential energy (V), and of the fractions of four-fold and five-fold coordinations (C_4 and C_5, respectively), for an *a*-Si film grown from the vapor with random-incidence directions, onto a Si(111) substrate. The system was cooled to 300 K after the end of the growth process. Density in units of σ^{-3} ($\sigma=2.0951$ Å) and energy in units of $\varepsilon=50$ kcal/mol.

TABLE I. Structural characteristics of the amorphous films grown epitaxially by MD simulations of deposition from the vapor onto a Si(111) substrate, using a normal-incidence beam (ni) and random-incidence (ri) deposition. The film was cooled to 300 K after the growth process. The fraction of atoms with given coordination is denoted C_n and the average bond length of n-fold coordinated atoms is denoted by d (in Å). θ and ϕ_d are the average bond and dihedral angles, respectively, and ρ is the average density (in units of σ^{-3}, $\sigma=2.0951$Å). In the bottom part of the table, average bonding angles corresponding to the various coordination numbers are given. In calculating the coordination numbers, a cutoff value of 2.866 Å was used [determined as the first minima in the pair distribution function $g(r)$]. Standard deviations are given for the bond lengths and angles.

Coordination number	C_n(ni)	C_n(ri)	d(ni)	d(ri)
3	0.009	0.014	2.49±0.13	2.47±0.12
4	0.64	0.62	2.42±0.10	2.43±0.10
5	0.34	0.35	2.52±0.14	2.52±0.14
6	0.014	0.014	2.61±0.14	2.61±0.14
average	4.36	4.36	2.46±0.13	2.47±0.13
θ	107.0±19.0	106.9±19.5		
ϕ_d	30.3±12.4	29.8±12.1		
ρ	0.472	0.457		

Coordination number	θ(ni)	θ(ri)
3	104.1±15.6	104.4±12.7
4	108.8±11.5	108.6±12.6
5	105.2±24.3	105.3±24.2
6	102.9±28.2	102.8±28.5

mation of the voids involves a spontaneous (stochastic) development of a morphological inhomogeneity at the surface of the films [see Fig. 11(a)] which perpetuates and grows by shadowing of the density-deficient region, driven by the dynamical attractive interaction between the impinging particles with the film atoms and the low mobility of atoms on the surface of the film [see Figs. 11(b) and 11(c)]. As is seen in Fig. 11(d), the cavity which formed in this manner (of diameter ~10 Å) is eventually capped off upon further deposition, and later on another one develops [Fig. 11(e)–11(h)].

We note that the presence of tubular voids of this nature has been deduced from experimental studies of the microstructure of amorphous semiconductors.[29,31] We believe that the mechanisms of formation of such defects found from our simulations are valid for more extended systems under similar deposition conditions.

The profiles of the system (cooled to 300 K) shown in Fig. 12 appear to be uniform throughout the thickness of the film (apart from the interfacial region at the crystalline substrate to amorphous film interface; see discussion in Sec. III A), although, as we demonstrated above (see Fig. 11), the system contains voids. Structural characteristics of the a-Si film are given in Table I. We note that the density of the film grown by random-incidence deposition ($0.457\sigma^{-3}$, $\sigma=2.0951$ Å) is lower (due to the voids) than that obtained via deposition at normal incidence, and is close to the density of crystalline Si at 300 K ($0.455\sigma^{-3}$). Other structural characteristics are similar to those of the film grown by a normal incident beam (see Table I).

IV. SUMMARY

In this study we investigated the growth modes of a-Si films via vapor phase and low-energy molecular-beam epitaxy, using molecular-dynamics simulations. In order to explore the dependencies of the growth mechanisms and of the structural and dynamical properties of the grown films on the deposition geometry, we have performed simulations of a-Si epitaxial film growth on a Si(111) substrate using the Stillinger-Weber interaction potentials[53] and employing three different incidence geometries: (i) incidence along the normal to the substrate, (ii) deposition using an atomic beam directed at 60° from the normal to the substrate, and (iii) a random-incidence geometry, where the impinging particles are released at random directions with respect to the substrate normal. In these simulations, special precautions were taken (see Sec. II) in order to avoid excess heating of the surface region of the growing film due to interaction with the incident particles (whose initial energy when released from the planar source above the substrate is $3k_BT_{cm}/2$, where T_{cm} is the crystalline melting temperature). In this way we modeled the main mechanisms and structural characteristics of a-Si film growth where limited surface diffusion plays an important role. We believe that the microstructural features which we observe are faithfully simulated since the physical size of the simulated system is much larger than the range of the interatomic interactions. Dynamical simulations of larger and more complex growth morphologies would require a much larger computational effort.

The results of our simulations can be summarized as follows.

(a) The *a*-Si film growth by MBE with the particle beam directed along the normal to the substrate is characterized by a uniform density distribution ($\rho=0.472\sigma^{-3}$, $\sigma=2.0951$ Å) with 64% of the atoms possessing four-fold coordination and 34% in five-fold coordination (see Table I). The uniformity of the amorphous film grown for this geometry (i.e., the absence of well-defined voids or columnar microstructure) is related[7] to the reduced tendency for the formation of such microstructures for small angles of incidence with respect to the normal to the substrate and to the short-range nature of the interaction potentials.[53] The static structure factor $[S(k)]$ calculated[32] from the pair distribution function $[g(r)]$ for the grown *a*-Si film (which was cooled to 300 K after the termination of the growth process) agrees well with that obtained from diffraction experiments[32] (see Fig. 13), as well as with $S(k)$ calculated for a bulk *a*-Si sample prepared previously[52] by slow cooling of the melt. The density of vibrational modes, $D(\omega)$, for the film (see Fig. 14, dashed line), obtained by a Fourier transformation of the particles' velocity autocorrelation function, is in general correspondence with that obtained from experiment,[71] although the level of agreement is inferior compared to $D(\omega)$ calculated for bulk *a*-Si, prepared via slow cooling of the melt.[52]

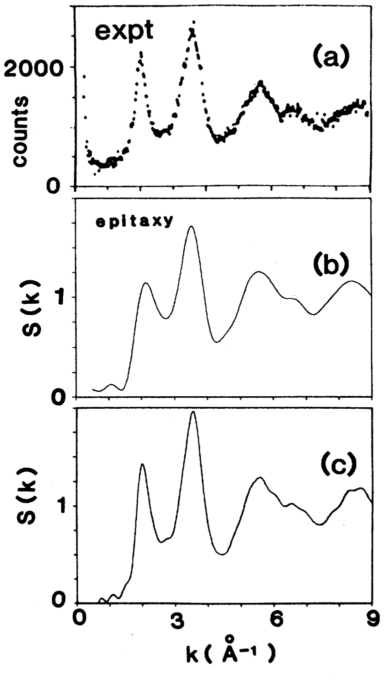

FIG. 13. Static structure factor $S(k)$ from experiment (Ref. 32) [in (a)] and for the *a*-Si films obtained via deposition from the vapor [in (b)]. The structure factors for the films grown under normal- and random-incidence deposition conditions are essentially identical. In addition, $S(k)$ for a bulk *a*-Si system prepared by slow cooling from the melt (Ref. 52) is shown for comparison in (c). The wave vector k, is in units of Å^{-1}.

(b) Deposition using a particle beam directed at 60° with respect to the surface normal results in a columnar microstructure, with intercolumnar voids. Using a column-orientation distribution function, we determine that the distribution of orientations of the intercolumnar voids peaks at ~41°, in agreement with the value obtained by the "tangent rule." The growth mechanism of the columnar structure involves initial nucleation of two-dimensional islands on the crystalline substrate

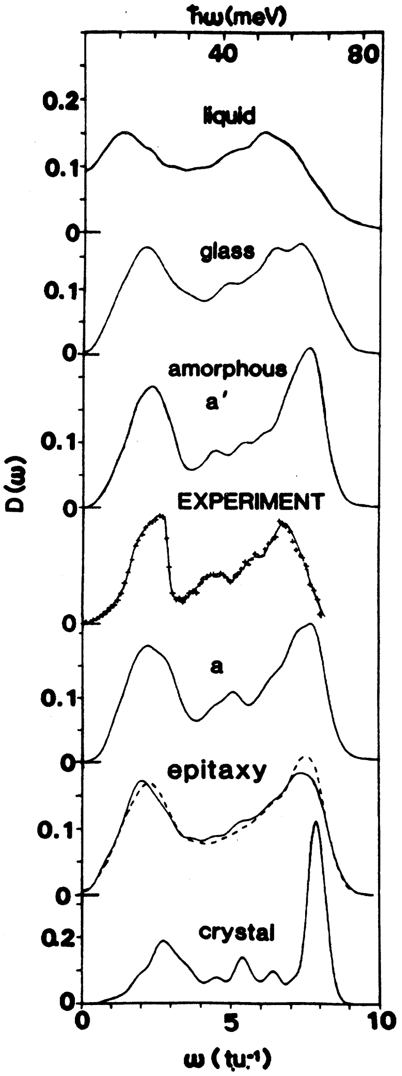

FIG. 14. Density of vibrational states, $D(\omega)$, for the *a*-Si film grown epitaxially by deposition using a normal incident beam (dashed line) and via deposition at random-incidence directions (solid line). In addition, we show $D(\omega)$ determined experimentally (Ref. 71), as well as the densities of states for bulk *a*-Si obtained by an indirect preparation procedure (Ref. 49) [(a')] and via slow cooling from the melt (Ref. 52) [(a)]. The densities of states for simulated room-temperature crystal and glass and for a liquid simulated at the melting point (Ref. 49) are shown for comparison. The frequency ω is given in units of the inverse of the time unit, t.u. $=7.66\times10^{14}$ sec.

which provide the nuclei for growth of three-dimensional clusters. The columnar growth is governed by geometrical and dynamical interaction factors, resulting in shadowing of the intercluster regions and the development of intercolumnar voids. The pronounced tendency for development of columnar structure for this angle of incidence and the apparent agreement with the tangent rule are related[7] to the small mobility of atoms deposited on the film and the short-range nature of the interaction potentials.[53]

(c) Random-incidence deposition results in growth of an *a*-Si film containing microvoids (whose diameter in our simulations is ~ 10 Å). The density of the grown film ($\rho = 0.457\sigma^{-3}$, $\sigma = 2.0951$ Å; see Table I) is lower (due to the voids) than that of the film grown via normal incidence [see conclusion (a)] and is comparable to that of the crystal ($\rho = 0.455\sigma^{-3}$) at 300 K. Other structural and dynamical characteristics of the film are similar to those of the film grown via normal-incidence deposition (see Table I and Figs. 13 and 14).

(d) The structure of the interfacial film (regardless of the deposition geometry) in the vicinity of the crystalline substrate exhibits, over a region of ~ 8 Å, partial crystalline and amorphous character, originating from crystalline intrusions embedded in an amorphous environment.

(e) Common to all the vapor-phase-epitaxial–growth systems investigated in this paper are the fast rate (~ 2 psec) of dissipation of the kinetic energy of the low-energy incident particles upon attachment to the surface, and the lack of significant diffusion on the surface. These results are in contrast to those obtained for a smooth crystalline-silicon surface,[26] and are due to the enhancement of the collisional energy transfer rates of particles impinging on disordered or amorphous substrates and the strong local bonding, characteristic of covalent materials.

ACKNOWLEDGMENTS

This work was supported by the U.S. Department of Energy under Grant No. FG05-86ER45234. The computations were performed on the Cray X-MP/48 at the National Magnetic Fusion Energy Computer Center, Livermore, CA.

---

[1] See reviews in Mater. Res. Soc. Bull. **13**, 18 (1988); **13**, 29 (1988).

[2] S. S. Lau and J. W. Mayer, in *Treatise on Material Science and Technology, Preparation and Properties of Thin Films,* edited by K. N. Tu and R. Rosenberg (Academic, New York, 1982), Vol. 24, Chap. 3; C. E. C. Wood, in *Physics of Thin Films* (Academic, New York, 1980), Vol. 2, p. 35; E. Kasper, Appl. Phys. A **28**, 129 (1982).

[3] (a) J. A. Thornton, J. Vac. Sci. Technol. **4**, 3059 (1986); (b) M. Sikkens, J. J. Hodgkinson, F. Horowitz, H. A. Macleod, and J. J. Wharton, Opt. Eng. **25**, 142 (1986).

[4] See articles in *Vapor Deposition,* edited by C. F. Powell, J. H. Oxley, and J. M. Blocher, Jr. (Wiley, New York, 1966).

[5] G. Honjo and K. Yagi, in *Current Topics in Materials Science,* edited by E. Kaldis (North-Holland, Amsterdam, 1980), Vol. 6, p. 195.

[6] *Epitaxial Growth,* edited by J. W. Matthews (Academic, New York, 1975).

[7] H. J. Leamy, G. H. Gilmer, and A. C. Dirks, in Ref. 5, p. 309.

[8] See J. A. Venables, Vacuum **33**, 701 (1983), and references therein.

[9] U. Landman, in *Computer Simulation Studies in Condensed Matter Physics: Recent Developments,* edited by D. P. Landau, K. K. Mon, and H.-B. Schuttler (Springer, Berlin, 1988), p. 108.

[10] U. Landman and W. D. Luedtke, in *Atomic Modeling in Materials: Beryond Pair-Potentials,* edited by V. Vitek (Plenum, New York, 1988).

[11] See articles in *Computer-Based Microscopic Description of the Structure and Properties of Materials,* Mater. Res. Soc. Symp. Proc. No. **63**, edited by J. Broughton, W. Krakow, and S. T. Pantelides (MRS, Pittsburgh, 1985).

[12] *Computer Simulations of Solids,* edited by C. R. A. Catlow and W. C. Machord (Springer, Berlin, 1982).

[13] F. F. Abraham, Adv. Phys. **35**, 1 (1986); J. Vac. Sci. Technol. B **2**, 534 (1984).

[14] U. Landman, W. D. Luedtke, and M. W. Ribarsky, in *New Materials Approaches to Tribology: Theory and Applications,* Mater. Res. Soc. Symp. Proc. No. 140, edited by L. E. Pope, L. L. Fehrenbacher, and W. O. Winer (MRS, Pittsburgh, 1989), p. 101.

[15] U. Landman, C. L. Cleveland, and C. S. Brown, Phys. Rev. Lett. **45**, 2032 (1980); U. Landman, C. L. Cleveland, C. S. Brown, and R. N. Barnett, in *Nonlinear Phenomena of Phase Transitions and Instabilities,* edited by T. Riste (Plenum, New York, 1982), p. 379.

[16] U. Landman, R. N. Barnett, C. L. Cleveland, and R. H. Rast, J. Vac. Sci. Technol. A **3**, 1574 (1985).

[17] C. L. Cleveland, U. Landman, and R. N. Barnett, Phys. Rev. Lett. **49**, 790 (1982).

[18] U. Landman, W. D. Luedtke, M. W. Ribarsky, R. N. Barnett, and C. L. Cleveland, Phys. Rev. B **37** 4637 (1988); **37**, 4647 (1988).

[19] U. Landman, W. D. Luedtke, R. N. Barnett, C. L. Cleveland, M. W. Ribarsky, E. Arnold, S. Ramesh, H. Baumgart, A. Martinez, and B. Khan, Phys. Rev. Lett. **56**, 155 (1986).

[20] See Ref. 7.

[21] M. Schneider, A. Rahman, and J. K. Schuller, Phys. Rev. Lett. **55**, 604 (1985).

[22] M. Schneider, A. Rahman, and J. K. Schuller, Phys. Rev. B **34**, 1643 (1986).

[23] M. Schneider, J. K. Schuller, and A. Rahman, Phys. Rev. B **36**, 1340 (1987).

[24] E. T. Gawlinski and J. D. Gunton, Phys. Rev. B **36**, 4774 (1987).

[25] K.-H. Muller, J. Appl. Phys. **61**, 2516 (1987); **58**, 2573 (1985).

[26] R. Biswas, G. S. Grest, and C. M. Soukoulis, Phys. Rev. B **38**, 8154 (1988).

[27] See reviews in Refs. 1–7 and references cited therein.

[28] J. S. Lannin, Phys. Today **41(7)**, 28 (1988), and references

therein.

[29]See A. Bienenstock, in *Amorphous and Liquid Semiconductors,* edited by J. Stake and W. Brenig (Wiley, New York, 1974), p. 49.

[30]B. G. Bagley, in *Amorphous and Liquid Semiconductors,* edited by J. Tauc (Plenum, New York, 1974), p. 1 (see, in particular, pp. 34–37).

[31]A. Chenevas-Paule and R. Bellissent, in *Tetrahedrally-Bonded Amorphous Semiconductors,* edited by D. Adler and H. Fritzsche (Plenum, New York, 1985), p. 11.

[32]T. A. Postal, C. M. Falco, R. T. Kampwirth, I. K. Schuller, and W. B. Yellon, Phys. Rev. Lett. **45**, 648 (1980).

[33]A. Chenevas-Paule, R. Bellissent, M. Roth, and J. I. Pankove, J. Non.-Cryst. Solids **77-78**, 373 (1986).

[34]A. J. Craven, A. J. Patterson, A. R. Long, and J. I. B. Wilson, J. Non-Cryst. Solids **77-78**, 217 (1986).

[35]P. D. Antonio and J. H. Konnert, Phys. Rev. Lett. **43**, 1161 (1979).

[36]N. J. Shevchik and W. Paul, J. Non-Cryst. Solids **16**, 55 (1974).

[37]B. A. Movchan and A. V. Demchishin, Phys. Met. Metallogr. **28**, 83 (1960).

[38]J. M. Nieuwenhuizen and H. B. Haanstra, Philips. Tech. Rev. **27**, 87 (1966).

[39](a) H. J. Leamy and A. G. Dirks, J. Appl. Phys. **44**, 3430 (1978); (b) A. G. Dirks and H. J. Leamy, Thin Solid Films **47**, 219 (1977).

[40]N. G. Nakhodkin and A. I. Shaldervan, Thin Solid Films **10**, 109 (1972).

[41]J. E. Yehoda, B. Yang, K. Vedam, and R. Messier, J. Vac. Sci. Technol. A **6**, 1631 (1988), and references therein.

[42]*The Physics of Hydrogenated Amorphous Silicon,* edited by J. D. Joannopoulos and G. Lucovsky (Springer-Verlag, New York, 1984).

[43]J. Shinar, R. Shinar, S. Mitra, M. L. Albers, H. R. Shanks, and T. D. Moustakas, in *Amorphous Silicon Semiconductors—Pure and Hydrogenated,* edited by A. Madan, M. Thompson, D. Adler, and Y. Hamakawa, Mater. Res. Soc. Symp. Proc. No. 95 (MRS, Pittsburgh, 1987), p. 183.

[44]R. Messier, and R. C. Ross, J. Appl. Phys. **53**, 6220 (1982).

[45]J. S. Lannin, in *Disordered Semiconductors,* edited by M. Kastner and G. A. Thomas (Plenum, New York, 1987), p. 283.

[46]R. Biswas, G. S. Grest, and C. M. Soukoulis, Phys. Rev. B **36**, 7437 (1987).

[47]K. Ding and H. C. Andersen, Phys. Rev. B **34**, 6987 (1986).

[48]M. D. Kluge, J. Ray, and A. Rahman, Phys. Rev. B **36**, 4234 (1987).

[49]W. D. Luedtke and U. Landman, Phys. Rev. B **37**, 4656 (1988).

[50]R. Car and M. Parrinello, Phys. Rev. Lett. **60**, 204 (1988).

[51]P. Kelieres and J. Tersoff, Phys. Rev. Lett. **61**, 562 (1988).

[52]W. D. Luedtke and U. Landman, Phys. Rev. B **40**, 1164 (1989).

[53]F. H. Stillinger and T. A. Weber, Phys. Rev. B **31**, 5262 (1985).

[54]R. Biswas, J. Kwon, A. M. Bouchard, C. M. Soukoulis, and G. S. Grest, Phys. Rev. B **39**, 5101 (1989).

[55]A. Guiner, G. Fournet, C. B. Walker, and K. L. Yudowitch, *Small Angle Scattering of X-Rays* (Wiley, New York, 1955).

[56]D. Henderson, M. H. Brodsky, and P. Chaudhari, Appl. Phys. Lett. **25**, 641 (1974); S. Kim, D. J. Henderson, and P. Chaudhari, Thin Solid Films **47**, 155 (1977).

[57]P. Meakin, P. Ramantal, L. M. Sander, and R. C. Ball, Phys. Rev. A **34**, 5091 (1986).

[58]P. Meakin, Phys. Rev. A **38**, 994 (1988).

[59]S. Lichter and J. Chen. Phys. Rev. Lett. **56**, 1396 (1986).

[60]T. Hashimoto, K. Okamoto, K. Hare, M. Kamiya, and H. Fujiwara, Thin Solid Films **91**, 145 (1982).

[61]O. Geszti, L. Gosztola, and E. Seyfried, Thin Solid Films **136**, L35 (1986); J. Non-Cryst. Solids **90**, 315 (1987).

[62]A. Barna, O. Geszti, L. Gosztola, and E. Seyfried, in *Defects in Glasses,* edited by F. L. Galeener, D. L. Griscom, and M. J. Weber, Mater. Res. Soc. Symp. Proc. No. 61 (MRS, Pittsburgh, 1986), p. 367.

[63]F. F. Abraham and I. P. Batra, Surf. Sci. **163**, L752 (1985).

[64]J. Q. Broughton and X. P. Li, Phys. Rev. B **35**, 9120 (1987).

[65]F. F. Abraham and J. Q. Broughton, Phys. Rev. Lett. **59**, 64 (1987).

[66]Y. Singh and F. F. Abraham, J. Chem. Phys. **67**, 384 (1977).

[67]D. Henderson, F. F. Abraham, and J. A. Barker, Mol. Phys. **31**, 291 (1976).

[68]F. F. Abraham, J. Chem. Phys. **68**, 713 (1978).

[69]J. W. Broughton, A. Bonissent, and F. F. Abraham, J. Chem. Phys. **74**, 29 (1981).

[70]J. Q. Broughton and G. H. Gilmer, J. Chem. Phys. **84**, 5759 (1986); **84**, 5749 (1986).

[71]W. A. Kamitakahara, C. M. Soukoulis, H. R. Shanks, U. Buchenau, and G. S. Grest, Phys. Rev. B **36**, 6539 (1987).